Available online at www.sciencedirect.com
ScienceDirect
International Journal of Multiphase Flow 33 (2007) 557–573
International Journal of Multiphase Flow
www.elsevier.com/locate/ijmulflow

Validation of a numerical model for the simulation of an electrostatic powder coating process

U. Shah [a], C. Zhang [b], J. Zhu [a,*], F. Wang [a], R. Martinuzzi [b]

[a] Department of Chemical and Biochemical Engineering, The University of Western Ontario, London, Canada N6A 5B9
[b] Department of Mechanical and Materials Engineering, The University of Western Ontario, London, Canada N6A 5B9

Received 16 October 2004; received in revised form 14 November 2006

Abstract

Numerical modeling of a complete powder coating process is carried out to understand the gas-particle two-phase flow field inside a powder coating booth and results of the numerical simulations are compared with experimental data to validate the numerical results. The flow inside the coating booth is modeled as a three-dimensional turbulent continuous gas flow with solid powder particles as a discrete phase. The continuous gas flow is predicted by solving Navier–Stokes equations using a standard k–ε turbulence model with non-equilibrium wall functions. The discrete phase is modeled based on a Lagrangian approach. In the calculation of particle propagation, a particle size distribution obtained through experiments is applied. The electrostatic field, including the effect of space charge due to free ions, is calculated with the use of the user defined scalar transport equations and user defined scalar functions in the software package, FLUENT, for the electrostatic potential and charge density.

Keywords: Powder coating; Numerical simulation; Lagrangian method; Space charge density; κ–ε Turbulence model; Electrostatics

1. Introduction

Powder coating is considered a more economical and ecologically friendly process compared to wet painting due to the avoidance of solvents (Bailey, 1998). Electrostatic powder spray painting is of significant industrial interest since it offers many advantages and great flexibility. The powder coating process involves fluidization and transport of powder particles, which are charged and sprayed over an electrically earthed workpiece using a spray gun, and deposition of charged powder particles over the workpiece. When the required coating thickness is obtained, the workpiece is placed in an oven where the powder layer is fused to form a continuous film. Usually the coating process is carried out inside an enclosed space, a coating booth, to be able to reclaim the oversprayed powder and to keep work environment clean.

* Corresponding author. Tel.: +1 519 661 3807; fax: +1 519 850 2441.
E-mail address: jzhu@uwo.ca (J. Zhu).

0301-9322/$ - see front matter
doi:10.1016/j.ijmultiphaseflow.2006.12.001

The performance of a powder coating process is mainly measured by two parameters, the first pass transfer efficiency (FPTE) and the coating quality. The FPTE is generally defined as the ratio of the amount of powder deposited on the workpiece to the amount of powder sprayed from the spray gun. Powder properties such as particle size, particle size distribution, chemical composition, tribo and corona charging characteristics, electrical resistivity, hygroscopicity, fluidity and shape distribution all play significant roles on the performance of a powder coating process, such as FPTE, the uniformity of the coating film, adhesion and appearance (Mazumder et al., 1997). The uniformity of the coating film and appearance are the major issues for potential use of powder coating for high-end surface coatings, such as the large market of automobile top clear coats. Presently, the powder coating industry uses 30 μm or larger size particles. These coarse powders cannot provide very smooth surfaces finishes. As a result, the use powder coating in the automotive industry has been restricted to some underhood components and parts, such as hubcaps, door handles and radiators, and is generally not used for the more lucrative automotive top clear coat applications. Yanagida et al. (1996) reported that high-quality clear coating for the automotive industry is attainable using mean paint particle diameters around 10 μm. Industrial experiments carried out in our Powder Technology Research Centre have also shown that the use of 15 μm paint powder, if not agglomerated, results in excellent surface finish. Therefore, it is possible that powder coating can provide the required surface finishing and the cosmetic look required to penetrate the large potential market of automotive top clear coat using finer particles.

A major issue relating to the use of the fine powder is its fluidity. Fine powders tend to agglomerate and form clumps. Zhu and Zhang (2002) developed a technology to fluidize these fine particles and it is now possible to use fine powder in coating industries and replace liquid painting for high-end surface finishing. To this end, however, it is very important to study the flow field of the sprayed powder and air inside the coating booth to understand its influence on the performance of the coating process and to design appropriate operating conditions and geometric parameters of the coating booth for a given spray gun. Numerical simulations can be a very useful to investigate such flows and understand various underlying phenomena. Elmoursi (1989) studied the electrostatic field, under Laplacian condition, in the space between bell and the paint target as well as at their surface for the bell type electrostatic liquid spray-painting system. Later, this model was expanded to study the space charge effect of charged paint droplets (Elmoursi, 1992). It was found that the space charge tends to enhance particle deposition and also causes the spray pattern to expand. Woolard and Ramani (1995) developed a three-dimensional finite element model for predicting the electrostatic field. The model was used as a tool for predicting the effect of various parameters on the electrostatic field. Ali et al. (2000) developed a mathematical model for the electrostatic field of the corona powder coating system to simulate single particle trajectories for a given charge to mass ratio, particle diameter and initial position. It was found that as the charge to mass ratio increases the particle trajectory spread further out in the radial direction. So far, most efforts were to study the electrostatic field but not to completely model a coating process.

Bottner and Sommerfeld (2002) used computational fluid dynamics (CFD) to simulate a complete electrostatic powder coating process under the Laplace condition using two types of corona spray guns, a slit nozzle and a round nozzle with a dispersion cone, and two types of coating parts, a flat plate and a tube. A standard κ–ε turbulence model was used for the gas-phase flow. The results agree well with the experimental data for both the particle velocity field and the coating layer thickness. However, they ignored the effect of space charge on the electrostatic field and the effect of ion wind, which is generated by collisions between ions and molecules with neutral charge, on airflow field. Ye et al. (2002) simulated the electrostatic powder coating process using the commercial CFD code, FLUENT v5.2. The corona spray gun was used. They considered the influence of space charge due to charged particles on the overall electrostatic field, but ignored the effect of ion wind. The direct interaction between particles and the effect of the particle motion on the continuous phase were neglected. The numerical results were compared with the experimental data and good agreement was found for air velocities and coating layer thickness. Later, Ye and Domnick (2003) extended the above model to consider the space charge due to the free ions, but did not include the space charge due to charged particles and the effect of the particle motion on the continuous phase. They also included the influence of turbulence dispersion on the sprays, which was previously ignored. It was observed that the effect of the space charge is significant and it tends to increase the strength of the electrostatic field in the region between the two electrodes especially near the target, which enhances the particle deposition. They validated their model by

comparing the numerical results with the experimental data for ion current density, particle charge, particle size distribution and coating film thickness.

It is of importance to investigate the accuracy of the CFD predictions for particle velocity and diameter distributions at various locations inside the spray region. Such numerical model can then be used to study the effect of various operation conditions and geometric parameters on the coating efficiency and quality.

In this paper, a complete powder coating process was modeled and simulated using a commercial CFD code, FLUENT v6.1. The aims of this study are to: (1) model the electrostatic powder coating process with corona spray gun; (2) provide a better understanding of the gas–solid flow field in a powder coating booth, and (3) evaluate the accuracy of the numerical model used for the simulations. The ultimate objective of this research program is to optimize the operating and geometrical parameters of the coating booth to increase the coating efficiency and coating quality.

In this study, the effect of the space charge due to the free ions on the electrostatic field was included when solving the electrostatic field, but the effect of the space charge due to charged particles on the electrostatic field was ignored. The particle trajectories were solved using Lagrangian method. The continuous gas flow was simulated by solving Reynolds averaged Navier–Stokes equations with a standard κ–ε turbulence model. The predicted particle velocity profiles and diameter profiles were compared with experimental data. The comparisons were made at various locations inside the coating booth in order to evaluate the accuracy of the numerical results. Detailed information on the experiments can be found in the work by Wang et al. (2005).

2. Configuration of the experimental powder coating system

A typical powder coating process consists of a fluidized bed hopper, a powder transport line from the hopper to the spray gun, an electrostatic spray gun, a coating booth and the workpiece to be coated. The powder particles for coating are first fluidized in the fluidized bed hopper. These particles are pneumatically carried through a transportation line to the powder spray gun, charged by the spray gun, and then sprayed to the part to be coated in the spray booth. Since the coating part is grounded and the particles are charged, the particles adhere to the part. The coated part is then conveyed to the oven where the coating is cured to form a hardened surface.

The dimensions of the coating booth and the relative positions of the gun and coating part are shown schematically in Fig. 1. The sidewalls of the booth except the back wall, i.e. the right, left and front walls, had been removed to allow access with Phase Doppler Anemometry (PDA). A 3 cm diameter suction hole at the top

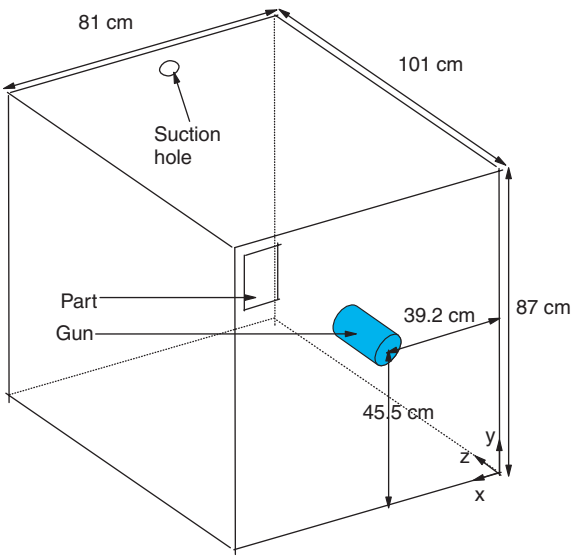

Fig. 1. Coating booth dimensions and spray gun position.

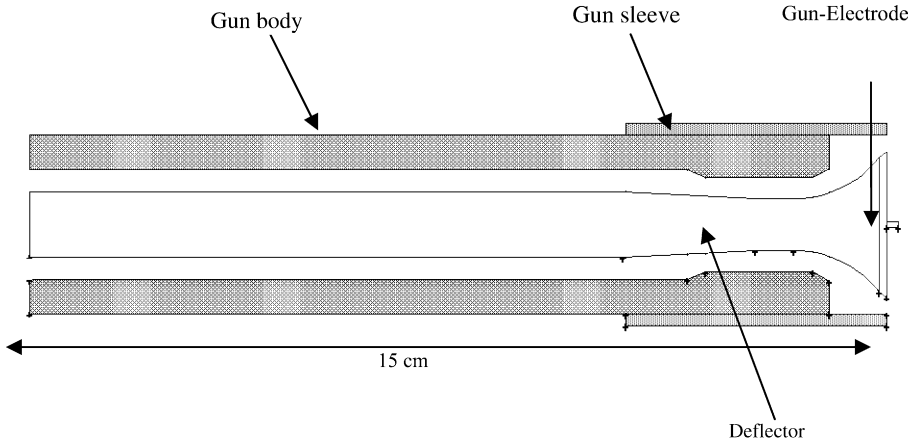

Fig. 2. Cross-sectional view of Nordson corona spray gun.

wall of the booth, as shown in Fig. 1, was used to maintain negative pressure inside the booth. So the powder particles will stay inside the booth. The back wall functions as a particle collector.

The 15 cm long corona spray gun as shown in Fig. 2 was used to spray the powder particles. The air fluidized powder flows through the annular space between the central trumpet-shaped cylindrical deflector and the outer gun body. The adjustable gun sleeve, which is used to adjust the powder flow pattern, was kept through out the study with the same position as shown in Fig. 2. The thin wire electrode, which is mounted at the center of the deflector plate, was applied with −50 kV to generate the electrostatic field between the gun-tip and the grounded coating part. The radius of the tip of the electrode was 0.3 mm. The 7.6 cm × 13.2 cm sized coating part was mounted 26 cm downstream of the gun-tip.

The particle size-velocity distributions were measured using a PDA system. Since PDA allows only for accurate size measurements of spherical particles and the particles are not expected to be spherical, particular care was taken to verify the validity of the measured distributions. The particle spray was sampled and analysed using a cascade impactor. Samples were also collected and observed under a scanning electron microscope (SEM) for particle shape and the formation of agglomerates as described in greater detail in Wang et al. (2005). The size distribution on the latter samples was also estimated based on the geometric mean particle diameters. While not spherical, the particle shapes were regular and generally rounded. For the PDA measurements, the particle distribution and validation rate were insensitive for sphericity validation below 80%. Based on 20 independent measurements, each containing 10,000 particle events, the PDA results showed a number averaged mean diameter (D_{10}) of 31 μm (standard deviation for the 20 samples of 4 μm), with 10% of the particles smaller than 11 μm and 90% of the particles smaller than 100 μm. For the SEM data, based on approximately 300 particles counted, the geometric mean was estimated to be approximately 34 μm with 10% of the particles smaller than 8 μm and 90% smaller than 70 μm. The nominal particle size as provided by the manufacturer is 35 μm.

3. Numerical modelling of the powder coating system

The air fluidized powder spray flow inside the coating booth was simulated as a two-phase flow with air as the continuous and the particles as the dispersed phase. In the present study, the particle volume fraction is less than 0.1% and hence the process is a dilute gas–solid two-phase flow in the regime of two-way coupling. The two-way interactions between the gas and particulate phases are included in the simulations through the drag source terms in the momentum equations for both phases. The effect of possible particle–particle interaction on the flow is neglected. The effect of the space charge due to free ions on the electrostatic filed was included in the transport equation for the electrostatic field. The effect of ion wind, which could have strong influence near the gun electrode region, on the airflow field is ignored, which means the electrostatic field affects the airflow only through its influence on particle trajectories by adding electrostatic body force on particles.

3.1. Gas flow

The gas (air) flow is considered three-dimensional, incompressible, steady and turbulent, and solved using the Reynolds averaged Navier–Stokes equations with a standard k–ε turbulence model. The governing equations for the gas phase are the conservation the mass and momentum equations as given in Table 1.

3.2. Electrostatic field

A high negative voltage is applied to the emitting electrode at the gun-tip to generate the electrostatic field between the electrode and the grounded electrode, the coating part. The electrostatic field can be described by a Poisson equation,

$$\nabla^2\phi = -\frac{\rho}{\varepsilon_0}, \tag{1}$$

where ρ is the space charge density and ε_0 is the electrical permittivity of the gas phase. The potential ϕ is related to the electrostatic field intensity, $\vec{E}$, according to

$$\vec{E} = -\nabla\phi. \tag{2}$$

The space charge represents the contribution of free ions and charged particles to the overall electrostatic field. The space charge due to charged particles was not considered in this study because earlier work (Bailey, 1998; Ye and Domnick, 2003) suggested that its contribution to the total space charge is 1/10th of the ionic space charge. The ionic space charge density, ρ, is related to the current density, $\vec{J}$. With the assumption of constant ion mobility, the correlation between $\vec{J}$ and ρ can be described as

$$\vec{J} = \mu_0\rho\vec{E} - D\nabla\rho, \tag{3}$$

where D is the diffusion coefficient. The value of ion mobility, μ_0, can be taken from 1.82×10^{-4} to 2.2×10^{-4} $\mathrm{ms^{-1}(Vm^{-1})^{-1}}$ (Ye and Domnick, 2003 and Anagnostopoulos and Bergeles, 2002). The value of 2.0×10^{-4} $\mathrm{ms^{-1}(Vm^{-1})^{-1}}$ was used in this study. The current density, $\vec{J}$, satisfies the following conservation equation:

$$\nabla\cdot\vec{J} = 0. \tag{4}$$

Table 1
Governing equations and auxiliary relations

Governing equations

Mass conservation equation

$\frac{\partial\overline{u_{ai}}}{\partial x_i} = 0$

Momentum conservation equations

$\frac{\partial}{\partial x_j}(\rho_a\overline{u_{ai}u_{aj}}) = -\frac{\partial p}{\partial x_i} + \frac{\partial}{\partial x_j}\left[\mu\left(\frac{\partial\overline{u_{ai}}}{\partial x_j} + \frac{\partial\overline{u_{aj}}}{\partial x_i}\right)\right] + \frac{\partial}{\partial x_j}(-\rho_a\overline{u'_{ai}u'_{aj}}) + \rho_a g_i + \rho_a F_D(u_{pi} - u_{ai})$

k–ε turbulence model

$\rho_a\bar{u}_{ai}\frac{\partial k}{\partial x_i} = \frac{\partial}{\partial x_i}\left[\left(\mu + \frac{\mu_t}{\sigma_k}\right)\frac{\partial k}{\partial x_i}\right] + G_k - \rho_a\varepsilon$

$\rho_a\bar{u}_{ai}\frac{\partial\varepsilon}{\partial x_i} = \frac{\partial}{\partial x_i}\left[\left(\mu + \frac{\mu_t}{\sigma_\varepsilon}\right)\frac{\partial\varepsilon}{\partial x_i}\right] + C_{1\varepsilon}\frac{\varepsilon}{k}G_k - C_{2\varepsilon}\rho_a\frac{\varepsilon^2}{k}$

Auxiliary relations

Drag force due to interaction between solid phase and gas phase

$F_D = \frac{18\mu}{\rho_p d_p^2}\frac{C_D Re}{24}$ where $Re_= \frac{\rho_a d_p|u_p - u_a|}{\mu}$

Drag coefficient

$C_D = \frac{24}{Re}(1 + b_1 Re^{b_2}) + \frac{b_3 Re}{b_4 + Re}$

where

$b_1 = \exp(2.3288 - 6.4581\phi + 2.4486\phi^2)$

$b_2 = 0.0964 + 0.5565\phi$

$b_3 = \exp(4.905 - 13.8944\phi + 18.4222\phi^2 - 10.2599\phi^3)$

$b_4 = \exp(1.4681 + 12.2584\phi - 20.7322\phi^2 + 15.8855\phi^3)$

The shape factor, ϕ, can be taken as 1, since the particles are close to spherical

Boussinesq hypothesis

$-\rho\overline{u'_{ai}u'_{aj}} = \mu_t\left(\frac{\partial\overline{u_{ai}}}{\partial x_j} + \frac{\partial\overline{u_{aj}}}{\partial x_i}\right) - \frac{2}{3}(\rho_a k)\delta_{ij}$

Turbulent viscosity

$\mu_t = \rho_a C_\mu\frac{k^2}{\varepsilon}$

Generation turbulent kinetic energy

$G_k = -\rho_a\overline{u'_{ai}u'_{aj}}\frac{\partial u_{aj}}{\partial x_i}$

Turbulent constants

$C_\mu = 0.09$, $C_{1\varepsilon} = 1.44$, $C_{2\varepsilon} = 1.92$

Turbulent Prandtl numbers

$\sigma_k = 1$, $\sigma_\varepsilon = 1.3$

Substituting Eq. (3) into Eq. (4) and combining with Eqs. (1) and (2), yields the following partial differential equation for the space charge density:

$$D\nabla^2\rho + \mu_0\nabla\varphi\cdot\nabla\rho = \frac{\rho^2\mu_0}{\varepsilon_0}. \tag{5}$$

Eqs. (1) and (5) were solved iteratively to obtain the electrostatic field. These equations were incorporated into the numerical model using the user defined scalar transport equations and user defined functions (Fluent UDF Manual, 2003).

The value of the space charge density at the corona electrode surface, ρ_0, which is the boundary condition for Eq. (5), was determined by

$$\rho_0 = -\frac{\varepsilon}{\Delta s}(E - E_0), \tag{6}$$

where E_0 is the magnitude of the onset field intensity at the corona surface, E is the magnitude of the field intensity at the cell neighbouring the corona electrode surface and Δs is the distance between the neighbouring cell and the electrode surface. If $E < E_0$, the value of ρ_0 was taken as zero at the corresponding surface of the electrode. E_0 was obtained according to the Peek's law:

$$E_0 = A\delta + B(\delta/r)^{1/2}, \tag{7}$$

where A and B are the empirical coefficients, δ the air relative density and r the radius of the corona electrode tip, which is 0.3 mm for this study. The values of A and B are 3.221×10^6 and 8.46×10^4 (Ye and Domnick, 2003), respectively.

3.3. Particle flow

The Discrete Phase Model (DPM) was selected to calculate the flow of the particulate phase since the gas–solid two-phase flow in the coating booth has been classified as a dilute flow. In DPM, the effect of particle–particle interactions on the solid flow was neglected since the volume fraction of the solid phase is very low in the powder coating system. Also, the powder particles were considered spherical and having smooth surfaces. The particle trajectories were predicted by integrating the equation of motion for the particles, which was based on the force balance on the particle and written in a Lagrangian reference frame. This force balance equates the particle inertia with the forces acting on the particle, and can be written (for i-direction in Cartesian coordinates) as

$$\frac{\mathrm{d}u_{\mathrm{p}i}}{\mathrm{d}t} = F_D(u_{\mathrm{a}i} - u_{\mathrm{p}i}) + g_i(\rho_{\mathrm{p}} - \rho_{\mathrm{a}})/\rho_{\mathrm{a}} + F_{\mathrm{E}i}/m_{\mathrm{p}}, \tag{8}$$

where $F_{\mathrm{E}i}$ is the electrostatic force component in i-direction, and m_{p} is the particle mass. The first and second terms on the right-hand side of Eq. (8) are the drag force and gravitational force, respectively. The electrostatic force due to the electrostatic field, $\vec{F}_{\mathrm{E}}$, is given by

$$\vec{F}_{\mathrm{E}} = q_{\mathrm{p}}\vec{E} + \frac{q_{\mathrm{p}}^2}{16\pi\varepsilon_0 a^2}\vec{n}_{\mathrm{p}}, \tag{9}$$

where q_{p} is the particle charge, a is the distance between the particle and the coating target, and $\vec{n}_{\mathrm{p}}$ is the unit vector from the location of the particle to the point on the coating target at which the distance between the particle and the coating part is the smallest. The first term on the right hand side of Eq. (9) is the Coulomb force and the second term is the image force, which has a significant contribution to the electrostatic force only when the particle is in the vicinity of the coating target.

The particle charging process is complicated and very much depends on the particle surface area. Due to the lack of available models for the charge to mass ratio, the average value of 1 μC/g, obtained from experiments, was used for the charge to mass ratio in the current study. It is important to notice here that the particles are considered carrying the charge only when they are inside the ion drift region. The ion drift region was defined with a fixed angle, θ, at the corona needle and in the direction of spray. $\theta = 60°$ based on the work by Sigmond

(1982) was used in the present study. To validate the assumption of $\theta = 60°$ the simulation for ion drift region with fixed angle $\theta = 70°$ was carried out and no significant difference in particle transfer efficiency was found.

The equation of motion for the particles, Eq. (8), was solved by stepwise integration over discrete time steps, which yields the velocity of the particle at each point along the trajectory. The particle trajectories were predicted by

$$\frac{dx_i}{dt} = u_{pi}. \tag{10}$$

Equations similar to Eqs. (8) and (10) were solved in each coordinate direction to predict the trajectories of the particles.

The discrete random walk (DRW) model (Fluent, 2001) was used to predict the turbulent dispersion of particles. In this approach, the dispersion was calculated by integrating the trajectory equations for individual particles, using an instantaneous fluid velocity, $\bar{u}_{ai} + u'_{ai}(t)$, along the particle path during the integration. The fluctuating velocity components are discrete piecewise constant functions of time. Their random value is kept constant over a period of time given by the characteristic lifetime of an eddy. Each eddy is characterized by a Gaussian distributed velocity fluctuation, u'_{ai}, and a time scale, τ_e. The fluctuating velocity component values are obtained assuming that they obey Gaussian probability distribution giving,

$$u'_{ai} = \varsigma\sqrt{\overline{u'^2_{ai}}}, \tag{11}$$

where ς is a normally distributed random number.

By computing the trajectory in this manner for a sufficient number of representative particles, the random effects of turbulence on the particle dispersion may be accounted for. Therefore, for statistical accuracy of the particle tracking, sufficient numbers of computational particles need to be tracked (Fluent, 2001 and Graham and Moyeed, 2002). Fig. 3 shows the mean, upper and lower confidence limits, obtained using 11 calculations and tracking 120,000 particles, of the predicted particle z-velocity profile along the horizontal (x) axis at 20 cm downstream of gun tip.

The PDA measurements provide the geometric diameters of particles. Therefore the number averaged mean diameter was selected for the input particle size distribution in order to compare the predicted particle diameter profile with the experimental one. Fig. 4 shows particle size distribution in terms of number frequency obtained using PDA. It shows that 92% of the total numbers of particles are having diameter less than 110 μm. Therefore, to save computation time, the particle size distribution with minimum particle diameter 2.5 μm, maximum 110 μm and mean, $D_{10} = 31$ μm was taken as the inlet condition in the numerical simulations for the considered coarse "regular" powder. The density of the particle is 1300 kg/m^3.

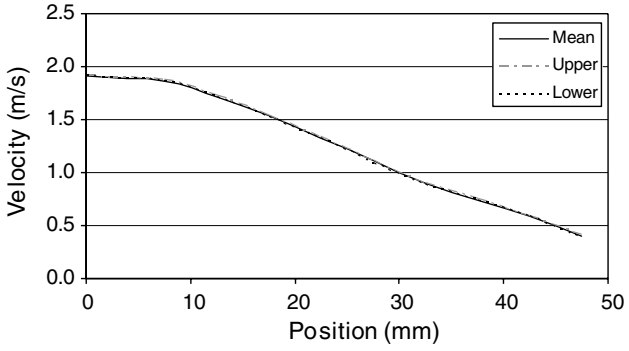

Fig. 3. Mean, upper and lower limits on the predicted particle z-velocity profile along the x-axis at 20 cm downstream of the gun tip (with electrostatic field and with coating part).

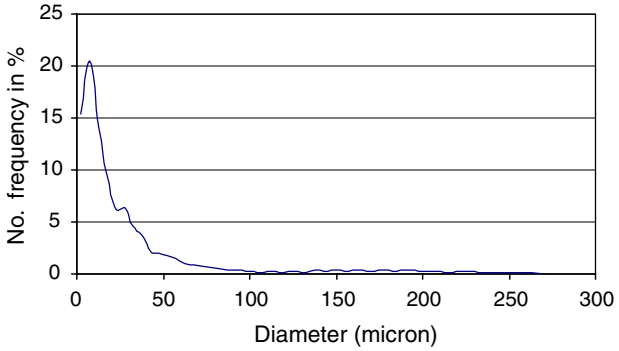

Fig. 4. Particle size distribution of coarse 'regular' powder for geometric diameter measured by PDA.

3.4. Boundary conditions

Table 2 shows the boundary conditions for the air flow, particle motion, and electrostatic field. It is important to mention that the air and particle inlet boundary conditions were defined at the spray gun inlet and block profiles for the velocities were assumed for both gas and solid phases at the gun inlet. The flows for both phases inside the spray gun have been included in the numerical simulations. The effect of the particle inlet velocity, which was set at the spray gun inlet, on the particle flow at the spray gun outlet was studied for different particle inlet velocities. It was found that there was no difference in the particle velocity profile at the spray gun outlet for different particle inlet velocities, reason being the spray gun length was sufficient to allow the flow to be fully developed at the gun outlet. It was assumed that all particles reaching the coating target will adhere, that is: no particles fall down or reflect back.

3.5. Computational mesh and solution procedure

The complex computational domain of the powder spay gun and coating booth of the powder coating system has been meshed using tetrahedral cells. The computational mesh has 1,200,000 hybrid cells after the solution adoption. The grid independency test was done with the further refinement of the mesh. Since the gradient values for ϕ from the neighboring cells to the corona electrode surface were required for solving Eq. (6), it is necessary to a have very fine mesh near the electrode and improve the representation of the circular surface near the corona electrode. This was obtained with surface boundary layers and solution refinement. Fig. 5 shows the mesh near the corona electrode.

The momentum and continuity equations were descritized using the second order upwind scheme and the standard pressure interpolation scheme was used for the pressure-field. The solution procedure for the governing equations is shown in Fig. 6.

Table 2
Boundary conditions

Air flow field	Pressure was set as zero (gage) at right, left and front walls Pressure is set as –14 kPa (gage) at the suction hole The total mass flow rate of the air at the spray gun inlet was set as 0.002 kg/s (8.67 m/s in velocity)
Particle motion	The total particle mass flow rate at the spray gun inlet was set as 0.04 kg/min The particle velocity at the spray gun inlet was set as 3 m/s Particles stay on the surface when they hit the coating part or bottom wall Particles bounce back when they hit the top wall Particles leave the booth when they hit the suction hole and the back wall
Electrostatic field	Voltage on corona electrode was set as −50 kV, grounded coating part was set as 0 kV The flux was set as zero on other boundaries

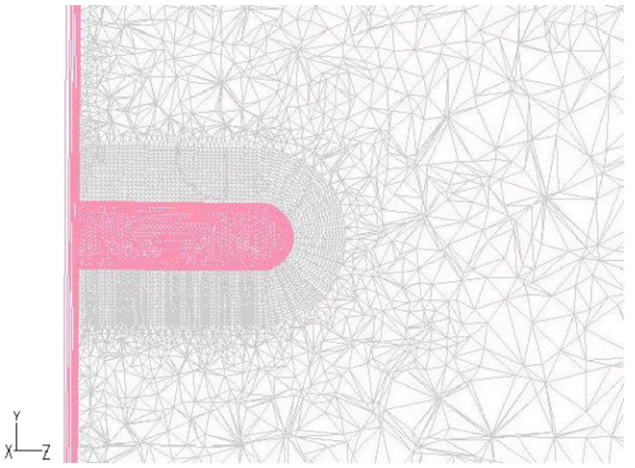

Fig. 5. Mesh in the vicinity of gun deflector.

4. Numerical results and the comparison with the experimental data

The following numerical simulations were carried out for the powder coating booth shown in Fig. 1:

(a) The gas–solid two-phase flows without the electrostatic field and without the presence of a coating part in the coating booth.
(b) The gas–solid two-phase flows without the electrostatic field and with the presence of a coating part in the coating booth.
(c) The gas–solid two-phase flows with the electrostatic field and with the presence of a coating part in the coating booth.

4.1. Gas flow

Figs. 7 and 8 show the predicted gas flow velocity vectors inside the coating booth and in the vicinity of the spray gun, respectively, with the electrostatic field and with a coating part in the coating booth. To allow a better visualization of the wake region near the spray gun deflector and the coating part, only the velocity vectors with magnitude from 0 to 5 m/s have been presented in the figures. The results clearly show the wake regions near the spray gun deflector front and the coating part. The mean gas velocity profiles at 2 mm, 20 mm and 150 mm downstream of the deflector front face are shown in Fig. 9 for the case with the electrostatic field and with a coating part. The trend of these results agrees well with that from Ye et al. (2002) although the values are slightly different since the spray gun geometry and inlet boundary conditions in the present work are different from those in Ye et al. (2002). Fig. 9 shows low velocities, even negative velocities, near the core region at the locations close to the spray gun deflector plate, i.e. at 2 mm and 20 mm from the deflector plate, because of the effect of the deflector plate wake. At 150 mm downstream of the deflector plate, the bell shaped gas velocity profile is developed as indicated in Fig. 9c.

4.2. Particle flow

The numerical results on the particle flow were obtained and compared with the experimental data to verify the performance of the numerical model. The average particle velocities and diameters at different positions on the horizontal (x) and vertical (y) axes inside the coating booth were compared with the experimental data. The measurement co-ordinate system is shown schematically in Fig. 10. The comparison was made for two

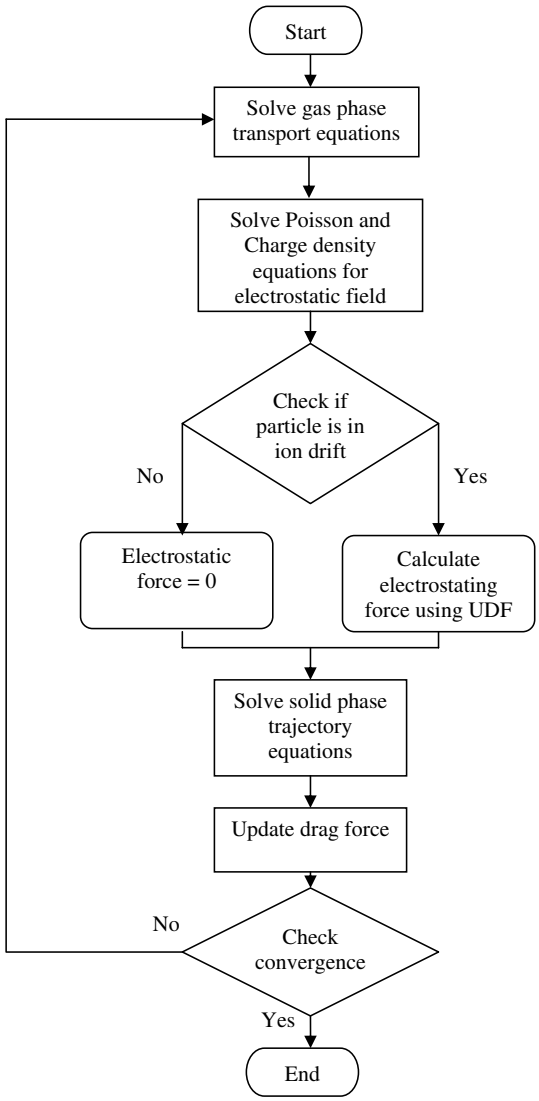

Fig. 6. Outline of numerical solution procedure.

velocity components, the z-velocity, which is the horizontal velocity component in the direction of the spray, and y-velocity, the vertical velocity component in gravity direction. The particle velocity presented in this study is the average velocity of all particles passing through the same point. To obtain the velocity, a small square surface of size 1 cm^2 was created inside the computational domain. The velocities of all the particles passing through that surface were averaged to obtain the average velocity.

The comparisons were made for flows without electrostatic field and with electrostatic field to validate the aerodynamic and electrostatic models, respectively, and also to understand the effect of the electrostatic field on the particle trajectories.

4.2.1. Particle velocity profiles: without the electrostatic field

During the coating process the grounded coating part is present in the spray zone. To check how the numerical model behaves under the conditions with and without a coating part, the comparisons were made for velocities under both of these conditions. This exercise also showed how the particle spray profile gets affected with the presence of the coating part.

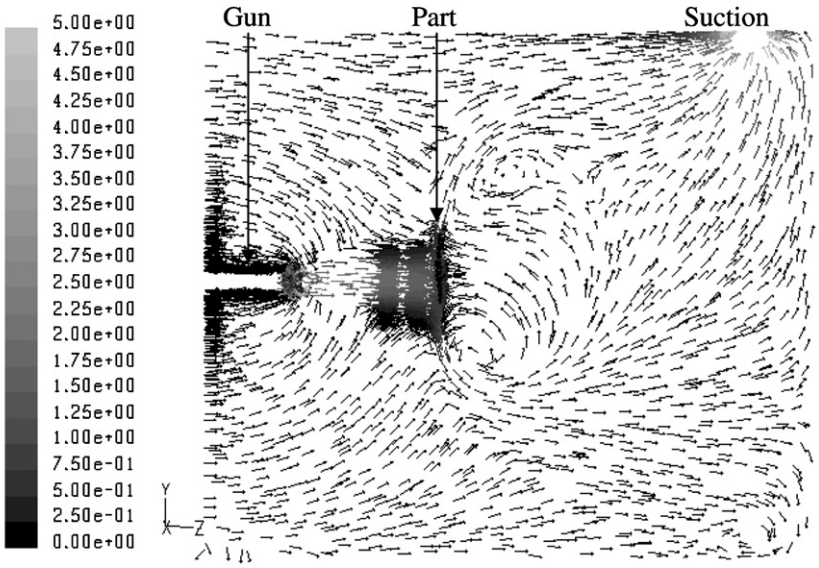

Fig. 7. Gas velocity vectors inside the coating booth on the y–z vertical plane at the gun center.

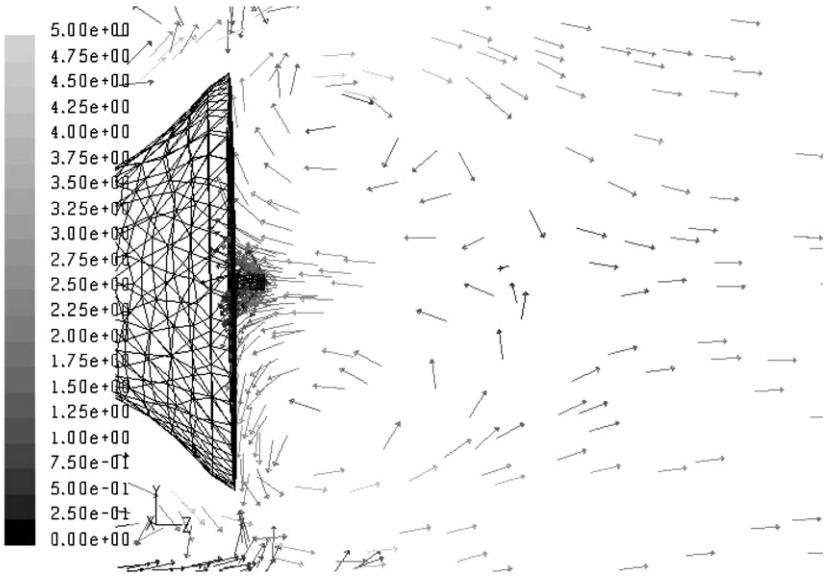

Fig. 8. Gas velocity vectors in the vicinity of the gun deflector plate.

4.2.1.1. Particle velocity profiles: without a coating part. The results presented in this section are for the straight jet condition, i.e. there was no coating part presented in the coating booth and no electrostatic field as well. The predicted average z-and y-velocities at different locations along the vertical (y) and horizontal (x) axes are compared with the experimental data as shown in Figs. 11 and 12, respectively.

Fig. 11 shows y-velocity, which is towards the gravitational direction, and z-velocity, which is towards the coating part, along the vertical (y) axis at 25 cm and 20 cm from the corona gun tip. These figures show a good agreement between the numerical results and experimental data for both y- and z-velocities. The bell shaped z-velocity profile indicates the particle spray pattern with higher velocity at the core region of the spray where the effect of the aerodynamic force is dominant and the velocity decreases with the spray radial distance. The

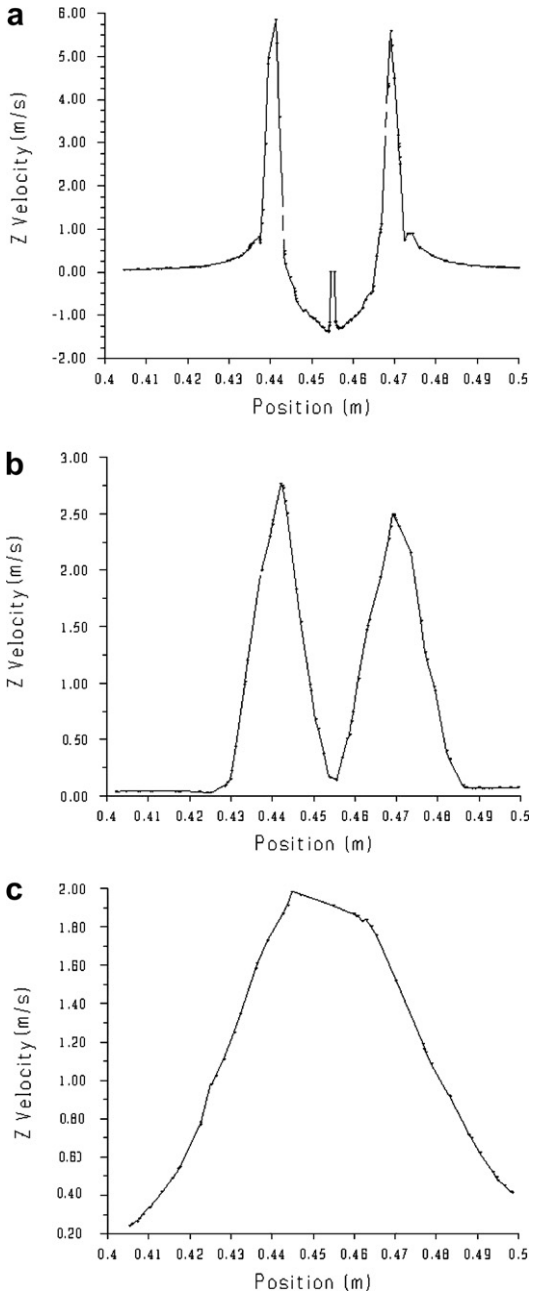

Fig. 9. Predicted gas velocity profiles along the vertical (y) axis at (a) 2 mm, (b) 20 and mm and (c) 150 mm downstream of the gun tip.

z-velocity profiles shown in Fig. 11 represent how the velocity profile changes with the distance from the spray gun. The velocity profiles are very indicative of the spray decay due to the spreading of the jet, which results in the radial velocities in the x- and y-directions and causes the decrease in the speed of the spray in the axial direction (the z-direction). Therefore, away from the spray gun, the shape of the particle velocity profile flattens. For example, the profile at 25 cm from the gun tip is more flat than that at 20 cm from the gun tip. The y-velocity at $y > 0$ (lower part of the jet) is positive, which means that the flow is downward, and the y-velocity at $y < 0$ (upper part of the jet) is negative, indicating that the flow is upward. This agrees with the velocity profile of a spray jet. The slightly higher downward particle velocity in the lower part of the jet comparing with that in the upper part of the jet might be caused by the gravity as well as the asymmetry in the flow field.

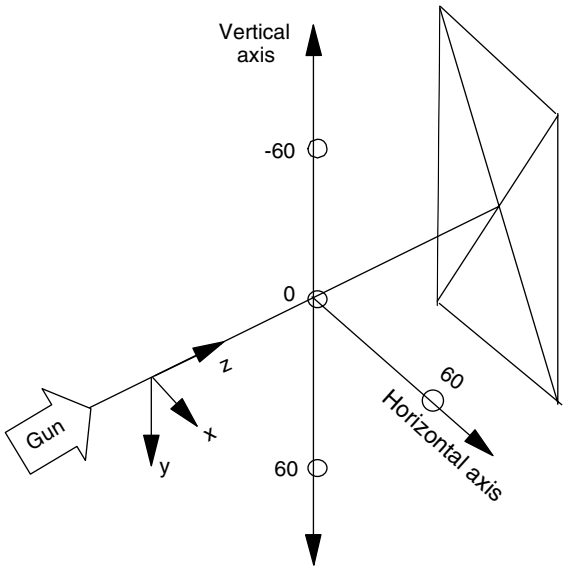

Fig. 10. The measurement axes.

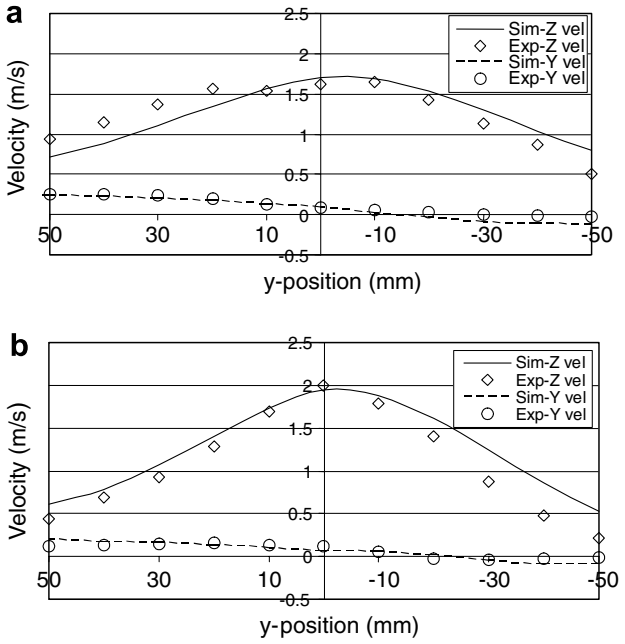

Fig. 11. Particle velocity profiles along the vertical (y) axis at (a) 25 cm and (b) 20 cm downstream of the gun tip (without electrostatic field and without a coating part).

Fig. 12 shows the comparison between the numerical results and experimental data for average particle velocities along the horizontal (x) axis at 25 cm and 20 cm from the gun tip. These comparisons also indicate that the numerical results agree well with the experimental data.

4.2.1.2. Particle velocity profiles: with a coating part. The numerical model is also examined for its ability to predict the particle velocity profiles when a coating part is placed in the coating booth and there is no electrostatic field by comparing the predicted results with the measured values. The coating part, 7.6 cm × 13.2 cm, was placed at 26 cm downstream of the gun tip.

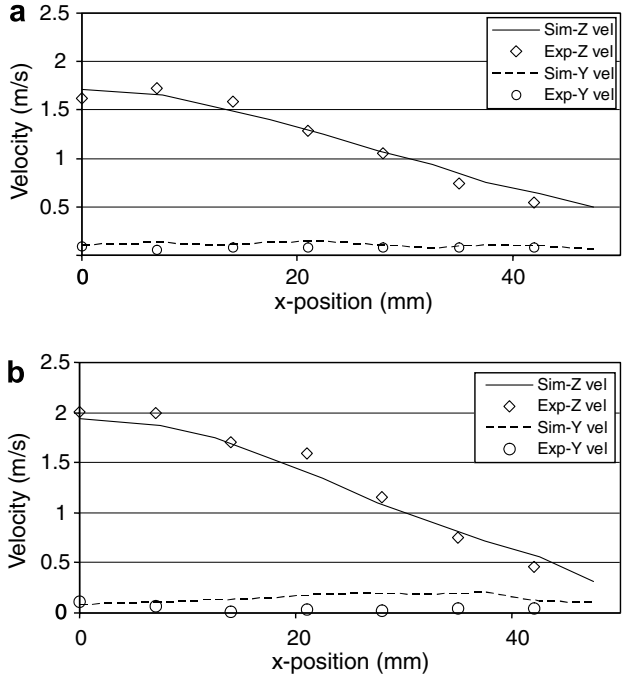

Fig. 12. Particle velocity profiles along the horizontal (x) axis at (a) 25 cm and (b) 20 cm downstream of the gun tip (without electrostatic field and without a coating part).

Fig. 13 shows the comparison between the numerical and experimental results for the velocity profiles along the vertical (y) axis at 25 cm and 20 cm downstream of the gun tip. The numerical model predicted the similar

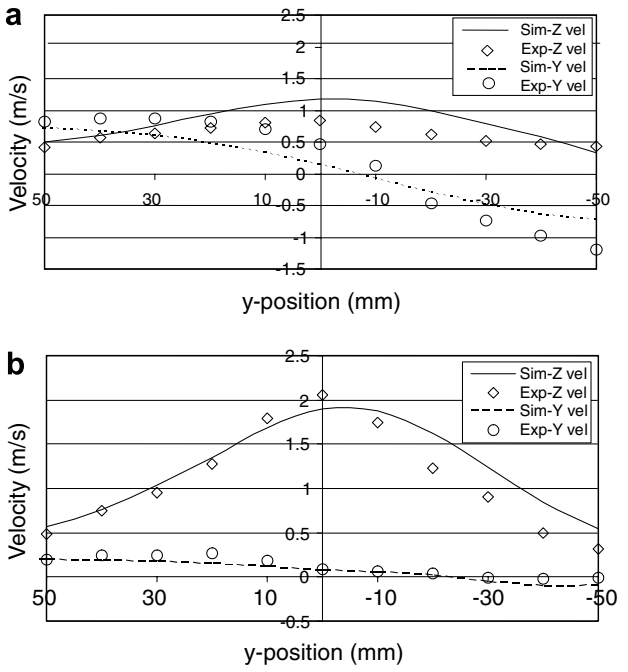

Fig. 13. Particle velocity profiles along the vertical (y) axis at (a) 25 cm and (b) 20 cm downstream of the gun tip (without electrostatic field and with a coating part).

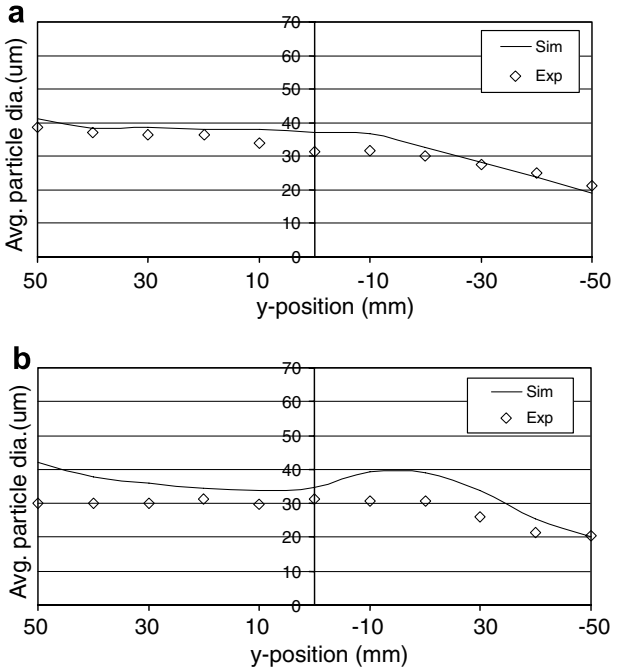

Fig. 14. Particle size profiles along the vertical axis (y) at (a) 25 and (b) 20 cm down-stream of the gun tip (without electrostatic field and with coating part).

pattern as it was seen in the measurements. In the numerical simulation, the assumption was made that all the particles hit to the coating target stay on the target while in the experiment some particles reflect back. In the comparison between the numerical and experimental results shown in Fig. 13, all negative particle z-velocities are removed from the experimental data. The discrepancy shown in Fig. 13a between the numerical results and experimental data at 25 cm from the gun tip, which is 1 cm from the coating part, could be due to the choice of standard κ–ε turbulence model that is often not suitable for resolving flows near stagnant boundaries.

It can be clearly seen by comparing the velocity profiles given in Figs. 11a and 13a that the presence of the coating part considerably lowers the particle z-velocity in the core spray region near the coating part, i.e. at 1 cm from the coating part and makes the z-velocity profile flatter, due to the blockage caused by the coating part (essentially a flat plate normal to the spray). However, the z-velocity away from the coating part, at 6 cm from the part, is not affected by the presence of the coating part. Therefore the z-velocity profiles shown in Figs. 11b and 13b are almost identical.

Fig. 14 shows the comparison for particle size distribution along the vertical (y) axis at 20 and 25 cm down-stream of the gun tip. The diameter distributions along the vertical axis show that the bigger particles tend to land on the bottom of the coating booth and smaller particles are at higher position inside the coating booth. This is because bigger particles are under higher gravitational force and tend to drift downwards while smaller particles follow the gas flow path and remain suspended for a longer time. The profile is more flat at 25 cm than it is at 20 cm because many big particles have fallen down. Both figures show good agreement between the predicted results and the experimental data. These observations suggest that the narrow distribution of feed powder with low average D_{10} could result in more uniform coating thickness in comparison with the feed powder with wider distribution, where bigger particles form thick coating in the bottom half of the coating object.

4.2.2. Particle velocity profiles: with electrostatic field

Fig. 15 shows the comparison for particle velocities along the horizontal (x) axis at 20 cm and 10 cm down-stream of the gun tip for the case with a coating part in the coating booth and with electrostatic field. These figures show a reasonable agreement between the numerical results and experimental data for both the z- and y-velocities except for the z-velocity at $x = 20$ mm and 10 cm from the gun tip, where the experimental value is

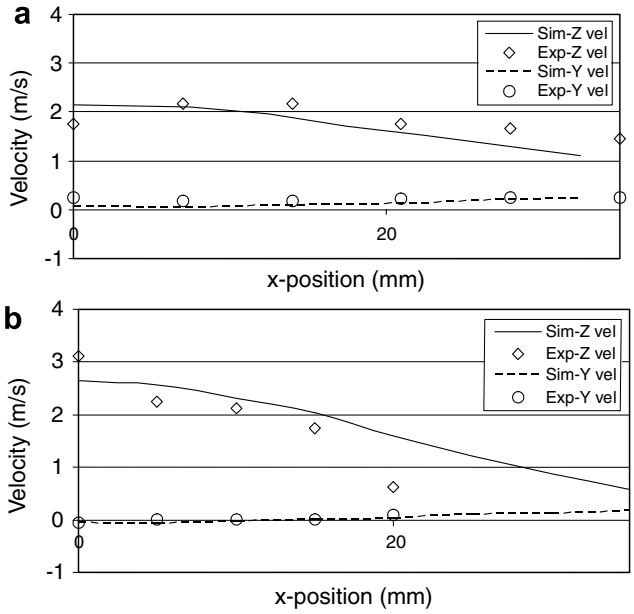

Fig. 15. Particle velocity profiles along the horizontal (x) axis at (a) 20 cm and (b) 10 cm downstream of the gun tip (with electrostatic field and with coating part).

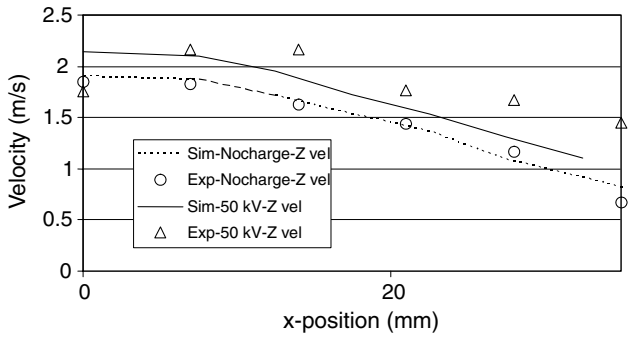

Fig. 16. Particle velocity profiles with and without electrostatic field on the horizontal (x) axis at 20 cm downstream of the gun tip (with coating part).

much lower than the simulation value as shown in Fig. 15(b). The comparison at 25 cm downstream of the gun tip, which is very close to the part, was not made since the back ionization affects the experimental data for particle velocities very close to the coating part and the numerical model used here does not account for the effect of back ionization.

The particle velocity profiles with the electrostatic field were compared with those without the electrostatic field to understand the effect of the applied electrostatic field on the particle motion and the trajectories of the particle. Fig. 16 shows the comparison along the horizontal (x) axis at 20 cm downstream of the gun tip. It shows that the electrostatic field causes an increase in the particle velocity towards the coating part, i.e. an increase in z-velocity.

5. Conclusions

The numerical model for the simulations of the gas and solid particle flows in a powder coating system was presented and its results were compared with the experimental data. It was found that the numerical model predicts quite accurately the particle velocities and average particle diameter at different locations inside the

coating booth when there was no electrostatic field. The numerical results showed similar effect of the electrostatic field on the flow field as that from experimental results. The differences between numerical results and experimental data, for the case of with the coating part and with electrostatic field, are most probably due to the assumption of constant charge to mass ratio and spherical shape of particles for this study. Thus, it should be important to numerically resolve particle charging using unsteady particle tracking or consider variable particle charge based on its diameter. In general, the presented simplified model appears useful for carrying out parametric studies considering different monosize powders.

The gas and particle flow fields could be understood by measuring the particle velocities and diameters at various locations inside the booth. Near the spray gun region the aerodynamic force is dominant and so the particles travel under its effect. Moving away from the spray gun, the electrostatic and the gravity force become dominant. The bigger particles tend to accumulate near the bottom of the coating booth and fine particles remain suspended with the gas flow for the longer time and finally being carried away through the suction hole. The electrostatic force is in the axial direction of spray and acts as an additional source to the particles' momentum. Thus, the electrostatic force plays an important role to increase the particle transfer efficiency. In addition, it affects the particle trajectories and expands it in the radial direction and finally concentrating on the target edges along the field lines.

The model gives a good insight into the process and can be used to understand the gas and particle flow fields for the fine powders. It can be used to understand the effect of various operating parameters such as the effect of particle size, applied voltage at the gun electrode, gas flow, particle loading, distance between the gun and the coating part etc. and optimize those for the maximum first pass transfer efficiency and better coating quality. The coating booth design also can be studied and optimized for the better containment of the powder particles to avoid the accumulation of powder near the corners of the booth, for defined gun geometry.

Acknowledgement

The authors are grateful to the Ontario Research and Development Challenge Fund for supporting this study.

References

Ali, F.S., Base, T.E., Inculet, I.I., 2000. Mathematical modeling of powder paint particle trajectories in electrostatic painting. IEEE Trans. Ind. Appl. 36, 992–997.

Anagnostopoulos, J., Bergeles, G., 2002. Corona discharge simulation in wire-duct electrostatic precipitator. J. Electrostat. 54, 129–147.

Bailey, A.G., 1998. The science and technology of electrostatic powder spraying transport and coating. J. Electrostat. 45, 85–120.

Bottner, C.U., Sommerfeld, M., 2002. Numerical calculation of electrostatic powder painting using the Euler/Lagrange approach. Powder Technol. 125, 206–216.

Elmoursi, A.A., 1989. Laplacian fields of bell-type electrostatic painting systems. IEEE Trans. Ind. Appl. 25, 234–240.

Elmoursi, A.A., 1992. Electrical characterization of bell-type electrostatic painting systems. IEEE Trans. Ind. Appl. 28, 1174–1181.

Fluent 6 User's Guide, 2001. Fluent Inc.

Fluent UDF Manual, 2003. Fluent Inc.

Graham, D.I., Moyeed, R.A., 2002. How many particles for my Lagrangian simulations? Powder Technol. 125, 179–186.

Mazumder, M.K., Wankum, D.L., Sims, R.A., Mountain, J.R., Chen, H., Pettit, P., Chaser, T., 1997. Influence of powder properties on the performance of electrostatic coating process. J. Electrostat. 40 & 41, 369–374.

Sigmond, R.S., 1982. Simple approximate treatment of unipolar space-charge dominated coronas: The Warburg law and the saturation current. J. Appl. Phys. 53 (2), 891–898.

Wang, C., Martinuzzi, R., Zhu, J., 2005. Experimental study of particle trajectory in electrostatics powder coating process. Powder Technol. 150 (1), 20–29.

Woolard, D.E., Ramani, K., 1995. Electric field modeling for electrostatic powder coating of a continuous fibre bundle. J. Electrostat. 35, 373–387.

Yanagida, K., Kumata, M., Yamamoto, M., 1996. J. Coat. Technol. 68, 47–56.

Ye, Q., Steigleder, T., Scheibe, A., Domnick, J., 2002. Numerical simulations of the electrostatic powder coating process with a corona spray gun. J. Electrostat. 54, 189–205.

Ye, Q., Domnick, J., 2003. On the simulation of space charge in electrostatic powder coating with a corona spray gun. Powder Technol., 250–260.

Zhu, J., Zhang, H., 2003. Fluidization Additives to Fine Powders, July 2002, US Patent, granted.